

# **Design of Small-Scale Wind Tunnel**

## **Final Project Assignment**

Computational Fluid Dynamics, 7.5 ECTS

Version 2.0

Elias Olofsson (elol0076@student.umu.se)

**Supervisor** Krister Wiklund  
**Examiner** Erik Zäll

## Abstract

Placeholder text.

# Contents

<b>1</b>	<b>Introduction</b>	<b>1</b>
<b>2</b>	<b>Theory</b>	<b>1</b>
2.1	Reynolds Averaged Navier-Stokes . . . . .	1
2.2	Boussinesq hypothesis . . . . .	2
2.3	Low Re $k-\varepsilon$ model . . . . .	2
2.4	Initial and boundary conditions . . . . .	4
2.5	Derived quantities . . . . .	4
<b>3</b>	<b>Method</b>	<b>5</b>
3.1	Wind tunnel fundamentals . . . . .	5
3.2	Modifications to wind tunnel geometry . . . . .	6
3.3	Measurement strategy . . . . .	6
3.4	Mesh specifications . . . . .	7
3.5	Mesh convergence study . . . . .	7
<b>4</b>	<b>Results</b>	<b>8</b>
4.1	Force plate sensor . . . . .	9
4.2	Smoke injector . . . . .	10
4.3	Comparison with reference data . . . . .	11
<b>5</b>	<b>Discussion</b>	<b>12</b>
<b>6</b>	<b>Conclusion</b>	<b>13</b>
<b>References</b>		<b>14</b>
<b>A</b>	<b>Appendix: Wind tunnel dimensions</b>	<b>i</b>
<b>B</b>	<b>Appendix: Contraction shape</b>	<b>iii</b>
<b>C</b>	<b>Appendix: Validation of modifications to geometry</b>	<b>iv</b>

# 1 Introduction

Wind tunnel tests are an important investigative tool in the field aerodynamics, since it presents an opportunity for detailed analysis and research of fluid phenomena [1], [2]. However, full-scale wind tunnels are often expensive to construct and require large spaces to be dedicated to them, making it impractical or even infeasible for smaller companies and research teams to build and operate them. A compromise is the usage of model-scale wind tunnels, which works on the principle of dynamical similarity through the matching of dimensionless quantities, e.g. Reynolds number [3].

Furthermore, the increase in available computational power during the last decades have made it possible to efficiently utilize Computational Fluid Dynamics (CFD) as a complement to traditional experimental techniques [3]. Nonetheless, for many real-life fluid flows, the best current computational methods for simulating fluid flow may still be insufficient or prohibitively expensive to employ [1]. Thus, while CFD can provide an important complement to experiments, wind tunnel tests remains a strong and essential tool for detailed analysis of complex fluid flow.

The company Hydroflux AB are interested in constructing a small-scale wind tunnel based on the general design by Mauro *et al.* [4] with inspiration for the contraction section from Sargison *et al.* [2] and Zanoun [5]. However, before such a wind tunnel is constructed, Hydroflux have asked us to investigate the effect on the main flow from interactions with certain sensor geometries, by using CFD-simulations of the wind tunnel. The sensors which are planned on being used in the real-life wind tunnel are a force plate sensor, used to measure lift forces of objects, and a smoke injector which can be used to create visual stream-lines in the wind tunnel, helping to visualize flow patterns.

Thus, the aim of this study is to understand and quantify the impact the sensor geometries have on the turbulence of the flow, both in the direct vicinity of the sensors, but also in the main bulk flow of the wind tunnel. Knowing these effects, it could be possible to optimize the sensor geometries such that the main flow is minimally affected by the presence of the sensors, and thus minimally disturbs the flow in any experiment of interest when the wind tunnel is operational.

# 2 Theory

## 2.1 Reynolds Averaged Navier-Stokes

The dynamics of a viscous, incompressible fluid are governed by the Navier-Stokes equations [3] which relate the forces and momenta of the fluid continuum and enforce mass conservation, as per

$$\rho \frac{\partial u_i}{\partial t} + \rho(\mathbf{u} \cdot \nabla) u_i = -\frac{\partial p}{\partial x_i} + \frac{\partial \tau_{ij}}{\partial x_j} + f_i \quad (1)$$

$$\rho \nabla \cdot \mathbf{u} = 0, \quad (2)$$

where the density  $\rho$  is assumed to be constant,  $u_i$  is the velocity and  $f_i$  is any external force. Furthermore, the viscous stress tensor  $\tau_{ij}$  is defined as

$$\tau_{ij} = 2\mu S_{ij} = \mu \left( \frac{\partial u_i}{\partial x_j} + \frac{\partial u_j}{\partial x_i} \right), \quad (3)$$

where  $\mu$  is the dynamic viscosity of the fluid and  $S_{ij}$  is the rate of strain tensor. While in theory this partial differential equation (PDE) describes the full dynamics of any incompressible Newtonian fluid, in practice and especially within an engineering context [3] we tend to work with simplified, modelled versions of the full Navier-Stokes equations. One popular approach are the Reynolds Averaged Navier-Stokes (RANS) equations, which can be derived from Eq.1-3 using a Reynolds decomposition like

$$\begin{cases} u_i = U_i + u'_i \\ p = P + p' \\ \tau_{ij} = T_{ij} + \tau'_{ij} \end{cases}, \quad (4)$$

where lowercase variables are the instantaneous values, uppercase variables are the mean values and the primed quantities are the fluctuations from the mean. Substituting these decomposed variables into Eq.1 and taking the expectation value of the entire equation, we can simplify the PDE using statistical rules and eventually arrive at RANS, as per

$$\rho \left( \frac{\partial U_i}{\partial t} + U_j \frac{\partial U_i}{\partial x_j} \right) = - \frac{\partial P}{\partial x_i} + \frac{\partial T_{ij}}{\partial x_j} + \frac{\partial R_{ij}}{\partial x_j} + \langle f_i \rangle \quad (5)$$

$$\frac{\partial U_i}{\partial x_i} = 0 \quad \frac{\partial u'_i}{\partial x_i} = 0, \quad (6)$$

where we have defined the Reynolds stress  $R_{ij}$  as

$$R_{ij} \equiv \rho \langle u'_i u'_j \rangle, \quad (7)$$

and in analogue to Eq.3, the bulk viscosity stress is defined as

$$T_{ij} = \mu \left( \frac{\partial U_i}{\partial x_j} + \frac{\partial U_j}{\partial x_i} \right). \quad (8)$$

## 2.2 Boussinesq hypothesis

However, due to the 'left-over' primed velocities in the definitions of Reynolds stress Eq.7, the system of equations is not closed. Thus in order to solve RANS (Eq.5-6), we need closure of the problem by finding a way to model the Reynolds stress. One way of achieving this is by adopting the Boussinesq hypothesis [6], which models the Reynolds stress as

$$R_{ij} \equiv - \langle \rho u'_i u'_j \rangle = \mu_t \left( \frac{\partial U_i}{\partial x_j} + \frac{\partial U_j}{\partial x_i} \right) - \frac{2}{3} \rho k \delta_{ij}, \quad (9)$$

where  $\delta_{ij}$  is the Kronecker delta,  $\mu_t$  is defined as the turbulence viscosity and  $k$  is the turbulence kinetic energy, defined as

$$k \equiv \frac{1}{2} \langle u'_i u'_i \rangle. \quad (10)$$

## 2.3 Low Re k- $\varepsilon$ model

Nonetheless, by adopting the Boussinesq hypothesis, we have not closed the system but rather moved the from the Reynolds stress tensor  $R_{ij}$  to the turbulent viscosity  $\mu_t$  and the turbulence

kinetic energy  $k$ . Thus, we need to choose a way to model these quantities, for which there are many options. The alternative we have chosen in here is the Low Re  $k-\varepsilon$  model [6], which employs the standard  $k-\varepsilon$  model with near wall modifications. The general form of the Low Re  $k-\varepsilon$  model is as per

$$\begin{aligned}\frac{Dk}{Dt} &= P_k - \tilde{\varepsilon} + D_k \\ \frac{D\tilde{\varepsilon}}{Dt} &= \frac{\tilde{\varepsilon}}{k} (f_1 C_{\varepsilon 1} P_k - f_2 C_{\varepsilon 2} \tilde{\varepsilon}) + D_\varepsilon + E,\end{aligned}\quad (11)$$

where  $P_k$  is defined as the production term of  $k$ ,

$$P_k \equiv \frac{R_{ij}}{\rho} \frac{\partial U_i}{\partial x_j} = \frac{\mu_t}{\rho} S^2. \quad (12)$$

Here,  $S^2$  relates to the rate of strain  $S_{ij}$  as

$$S^2 \equiv 2S_{ij}S_{ij}, \quad (13)$$

and  $D_k$  is the diffusion of  $k$

$$D_k \equiv \frac{\partial}{\partial x_j} \left[ \frac{1}{\rho} \left( \mu + \frac{\mu_t}{\sigma_k} \right) \frac{\partial k}{\partial x_j} \right]. \quad (14)$$

The turbulence dissipation rate of  $k$  is defined as  $\varepsilon$

$$\varepsilon \equiv \frac{\mu}{\rho} \left\langle \frac{\partial u'_i}{\partial x_j} \frac{\partial u'_i}{\partial x_j} \right\rangle, \quad (15)$$

which relates to  $\tilde{\varepsilon}$  as per

$$\varepsilon = \tilde{\varepsilon} + D. \quad (16)$$

The term  $D_\varepsilon$  in Eq.11, which gives the diffusion of  $\tilde{\varepsilon}$ , is defined as

$$D_\varepsilon \equiv \frac{\partial}{\partial x_j} \left[ \frac{1}{\rho} \left( \mu + \frac{\mu_t}{\sigma_\varepsilon} \right) \frac{\partial \varepsilon}{\partial x_j} \right], \quad (17)$$

and the turbulence viscosity model for the Low Re  $k-\varepsilon$  model is set to

$$\mu_t = f_\mu C_\mu \rho \frac{k^2}{\tilde{\varepsilon}}. \quad (18)$$

The constants  $C_{\varepsilon 1}$ ,  $C_{\varepsilon 2}$ ,  $C_\mu \sigma_k$ ,  $\sigma_\varepsilon$ ,  $E$ ,  $D$  as well as the damping functions  $f_1$ ,  $f_2$ ,  $f_\mu$  are typically inferred from experimental data, and there are many different alternative sets of constants and damping functions available. For this investigation, the chosen simulations software COMSOL implements the AKN model with the Low Re  $k-\varepsilon$  model, after its designers Abe, Kondoh, and Nagano [7] which specifies the damping functions as

$$\begin{aligned}f_\mu &= \left( 1 - e^{-l^*/14} \right)^2 \left[ 1 + 5 \text{Re}_T^{-3/4} e^{-(\text{Re}_T/200)^2} \right] \\ f_1 &= 1 \\ f_2 &= \left( 1 - e^{-l^*/3.1} \right)^2 \left[ 1 - 0.3e^{-(\text{Re}_T/6.5)^2} \right],\end{aligned}\quad (19)$$

where

$$l^* = \frac{\rho u_\varepsilon l_w}{\mu}, \quad \text{Re}_T \equiv \frac{\rho k^2}{\mu \varepsilon}, \quad u_\varepsilon = \left( \frac{\mu \varepsilon}{\rho} \right)^{1/4}, \quad (20)$$

in combination with the constants

$$C_{\varepsilon 1} = 1.5 \quad C_{\varepsilon 2} = 1.9 \quad C_\mu = 0.09 \quad \sigma_k = 1.4 \quad \sigma_\varepsilon = 1.4. \quad (21)$$

## 2.4 Initial and boundary conditions

Simulations performed during this investigation have used initial conditions in the entire domain as

$$\mathbf{u} = 0, \quad p = 0, \quad (22)$$

while letting COMSOL set automatically the initial values for the turbulence kinetic energy  $k$  and the turbulence dissipation rate  $\varepsilon$ . I have unfortunately not been able to inspect manually which numerical value COMSOL chooses internally but my assumption is that it is either zero or a constant value close to zero.

For the inlet into the domain, I have specified the boundary condition to have a constant, normal velocity into the domain determined by the volumetric flow rate  $Q_{in}$  and the inlet surface area. The turbulence intensity of the incoming flow is set to 5% at the boundary, and COMSOL automatically sets the turbulence length scale, of which I similarly have not been able to gain insight into. The outlet boundary condition is a simple pressure constraint at zero pressure, while simultaneously suppressing any backflow. On all other surfaces of the domain, a no-slip condition  $\mathbf{u} = 0$  is used.

## 2.5 Derived quantities

Quantities used to quantify the flow within the simulations have been the turbulence intensity

$$I \equiv \frac{u'}{U} \quad (23)$$

where  $u'$  is the root mean square of the turbulent velocity fluctuations and  $U$  is the mean velocity of the flow. Furthermore, we use the dimensionless quantities

$$U^+ \equiv \frac{U}{u_\tau}, \quad (24)$$

and

$$y^+ \equiv \frac{\rho u_\tau y}{\mu}, \quad (25)$$

which is a scale free and universal quantity for flow near walls due to its usage of the friction velocity

$$u_\tau \equiv \sqrt{\tau_w / \rho}, \quad (26)$$

where  $\tau_w$  is the wall shear stress. Similarly, we employ a dimensionless version of the turbulence kinetic energy  $k$ , as per

$$k^+ \equiv \frac{U}{u_\tau^2}. \quad (27)$$

Furthermore we have the Reynolds number

$$\text{Re} = \frac{\rho L U}{\mu}, \quad (28)$$

which balances the importance of the convective and viscous terms of the Navier-Stokes equations Eq.1, and its related quantity  $\text{Re}_\tau$  based on the friction velocity, as per

$$\text{Re}_\tau = \frac{\rho L u_\tau}{\mu}, \quad (29)$$

## 3 Method

### 3.1 Wind tunnel fundamentals

Any wind tunnel is composed of the same constituents components [1], a settling chamber with screens and/or honeycombs, a contraction section to increase velocity and uniformity of the flow, a testing chamber where the experiment takes place, a diffuser to recover static pressure and a drive system in the shape of a fan or turbine. The wind tunnel in question in this investigation is no exception, and the basic geometry of the wind tunnel was given by the Hydroflux AB as a CAD file, excluding the drive system of the wind tunnel, and is based on the design by S. Mauro *et al.* [4], with help of J.E. Sargison *et al.* [2] for the design of the contraction section. An overview of the wind tunnel can be seen in Fig.1.

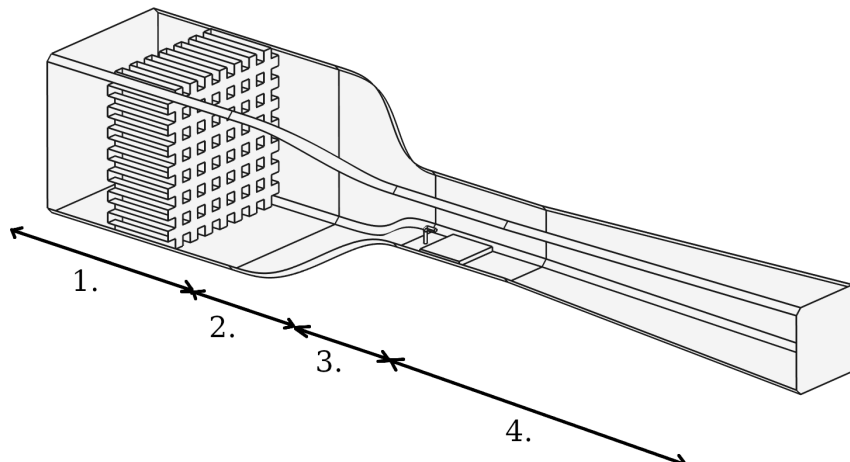


**Figure 1** – Left to right in flow direction: 1. Settling chamber, 2. Contraction, 3. Test section with force sensor and smoke injector, 4. Diffuser. Original CAD design supplied by Hydroflux AB, improved with slight alteration of the contraction shape and with the addition of  $45^\circ$  chamfers along the four edges of the wind tunnel in the direction of flow.

Here, we have the settling chamber with a coarse comb used as a flow conditioner, which minimizes transverse flows and breaks up large-scale flow irregularities [1], followed by the contraction section. Flow is sped up in the contraction, which is designed to maximize flow uniformity at the test section entrance while minimizing boundary layer separation [2]. Following the contraction, the flow enters the test section where the aerodynamic experiment is taking place. In Fig.1 one can see the force sensor and the smoke injector placed in the test section. On the one hand the test section should be long enough in order for turbulence fluctuations to dampen after the entrance, while on the other hand it should be short enough for boundary separation to not occur further down the test section [1]. Following the test section, the flow enters the diffuser which by its gradual widening reduces the flow-speed and decreases the pressure, which is beneficial and takes load of the drive system [1].

In this investigation, we have used fluid properties defined by Hydroflux AB, as given in Tab.1.

**Table 1** – Fluid and flow properties used in the simulation, specified by Hydroflux AB.

Parameter	Value	Comment
Density	1.184 kg/m <sup>3</sup>	Air 25°
Dynamic viscosity	$18.5 \cdot 10^{-6}$ Pas	Air 25°
Flow rate	0.05 m <sup>3</sup> /s	Determined by the choice of fan used to drive the flow
Turbulence intensity after settling chamber	1 – 5%	Depends on flow straightener, choice of screens, and the number of screens.

### 3.2 Modifications to wind tunnel geometry

While the original geometry was supplied by Hydroflux AB, two slight changes to the wind tunnel design have been made in this investigation. Firstly, as discussed by S. Mauro *et al.*[4], the optimal cross-sectional shape of the wind tunnel from a pure aerodynamic standpoint is for the tunnel to take a circular shape, which minimizes risks of flow separation at sharp edges. However, from a practical standpoint, a rectangular cross-sectional shape is much easier to construct and gives more surface area for experiments. A reasonable trade-off which [2] employs is to use 45° chamfers along the corners of the rectangular cross-section, and a similar approach has been used here in this investigation. Full details of the wind tunnel design and dimensions can be seen in Appendix A.

Secondly, a slight mistake was made in the original CAD-file supplied by Hydroflux AB. A small logical error in the Matlab-script for creation of the contraction shape in the wind tunnel resulted in the slight miss-alignment between the contraction section and the test section, yielding a small 'lip' at the intersection between test section and contraction. Since optimal conditions in the test section is minimal levels of turbulence and a uniform flow [1], such a small non-streamlined irregularity will have the possibility of creating unwanted flow separation and a boundary layer build-up in the test section. The Matlab-script used to generate the curvature which fixes this miss-alignment of the contraction section can be seen in Appendix B.

To validate claims of the improved wind tunnel design, tests were made to compare the performance of the empty wind tunnel using both the original and the modified design, of which the results can be seen in Appendix C. All further investigations in this study have been performed using the modified design.

### 3.3 Measurement strategy

Derived quantities from the performed simulations in this investigation have been taken from an assortment of cut-planes, cut-lines and cut-points at different locations within the wind tunnel. Velocity and turbulence intensity surface plots have been taken along 3D cut-planes as shown in Fig.2. The reason for using two cut-planes parallel to the flow was to be able to see the velocity and turbulence intensity within the small ducts of the rectangular comb of the settling duct, but to also graph the cross-section of the smoke injector centered in the wind tunnel. This proved to be a valid approach since differences were small in plotted quantities of the two parallel cut-planes. A third plane was placed perpendicular to the flow at the center of the test section.

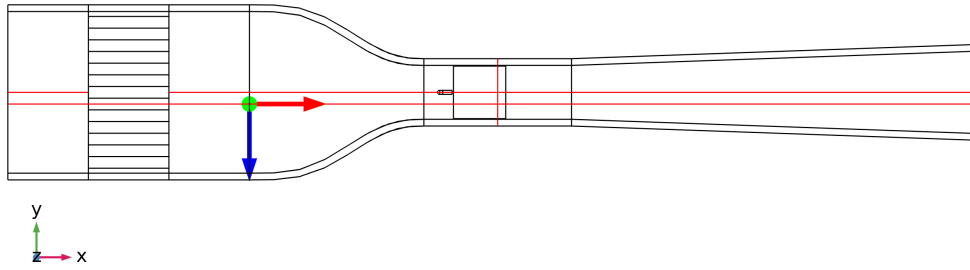


**Figure 2** – Cut-planes used for gathering of flow quantities. The two parallel cut-planes enabled graphing of quantities both in the small ducts of the flow comb in the settling chamber and at the center-line of the smoke injector.

For graphing the difference between the empty wind tunnel flow and with the force sensor and smoke injector added, three vertical cut-lines were used in the test section, as seen in Fig.3. They were placed along the center-line of the wind tunnel following the flow, and spaced out at 0.25, 0.5 and 0.75 times the length of the test section. The cut-points used for data-gathering

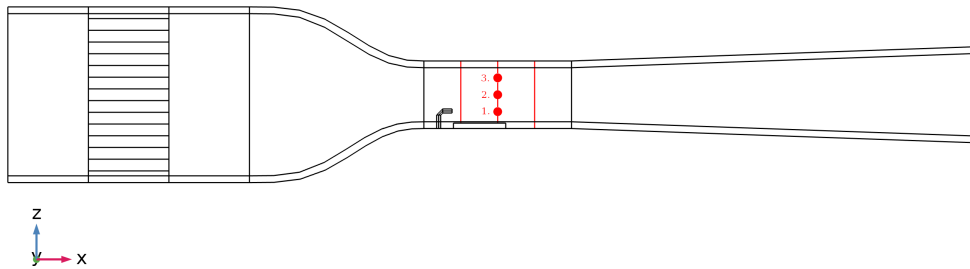


**Figure 3** – Cut-lines and cut-points used for gathering of flow quantities. Both the vertical cut-lines and the cut-points are centered in the transverse direction of the wind tunnel.

during the mesh convergence test can be seen in Fig.3, which are centered in the transverse orientation of the flow, ordered vertically at the center of the test section, vertically spaced at 0.25, 0.5 and 0.75 times the height of the test section.

### 3.4 Mesh specifications

During the comparison of simulations of the flow with the sensor, with the smoke injector and with an empty tunnel, the mesh used employed a global maximum element size of 0.0171 m, with a locally enforced maximum element size of 0.00698 m at all boundaries within the test section. In addition, all boundaries were specified to use 6 boundary layers with a thickness adjustment factor of 2, and locally constrained to use 10 boundary layers and a thickness adjustment factor of 1 at all boundaries within the test section. This gave me a simulation time around 40 min using a 4-core desktop computer.

### 3.5 Mesh convergence study

In order to determine if a given solution to a simulation is representative of the theoretical 'exact' solution, a mesh convergence study is performed. Here the given simulation is re-run a number of times with different quality and coarseness of its mesh, and we investigate the

convergence of some given parameters within the simulation. For this analysis, the reference case of an empty tunnel with the modified geometry was chosen, and the quantities inspected in each solution was the velocity magnitude  $U$  and pressure  $P$  at the three cut-points as specified in subsection 3.3. The maximum element size was set to 0.0132 m times a parameter `meshtest`, and for the local constraint at all boundaries within the test section, a maximum element size of 0.005235 m times a parameter `meshtest`. Then two consecutive batch sweeps were performed over the parameter `meshtest`, first in the range 1.0 to 3.0 in 10 linearly spaced increments, and later from 1.0 to 1.4 in 17 linearly spaced steps.

The result of the mesh convergence study can be seen in Fig.4. Here, one can see how the plotted quantities seem to stagnate as the number of degrees of freedom increases, as to be expected. For the final comparison between the empty tunnel, with the force sensor added and with the smoke injector added, the finest mesh in this study, or finer, was used.

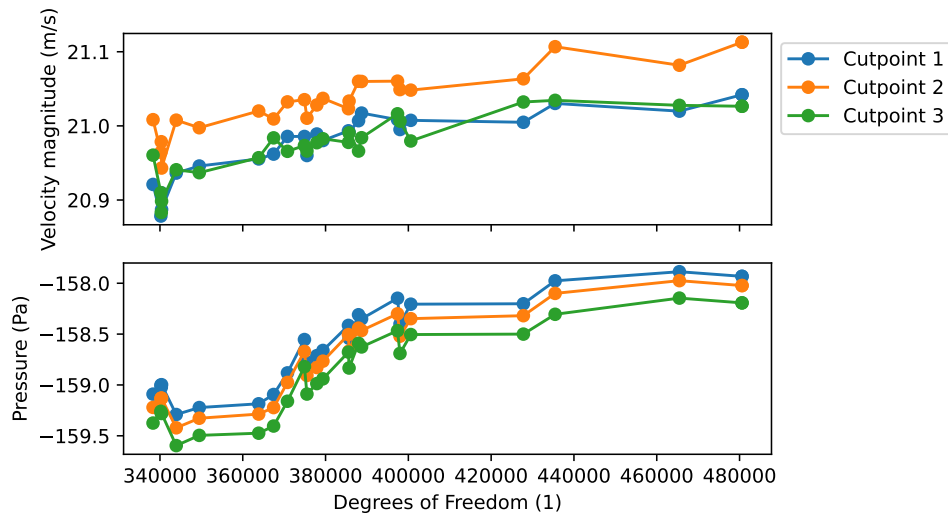


**Figure 4** – Mesh convergence study over two sequential batch sweeps. Quantities graphed in cut-points as specified in subsection 3.3.

During this study, I did not experience poor convergence while running the simulations, which I believe could be due to usage of the 'automatic' wall treatment feature in COMSOL, which smoothly switches between the Low Re  $k-\varepsilon$  model and the standard  $k-\varepsilon$  model with wall functions, depending on the local mesh resolution. Normally, the Low Re  $k-\varepsilon$  model requires a relatively fine mesh in order to have good convergence properties and one would have to increase the mesh quality when experiencing poor convergence. However, this never was a concern during this study.

## 4 Results

To address the aim of this investigative study and see how the flow changes in the wind tunnel as one adds the force sensor and smoke injector, three simulations were conducted at the finest mesh as described in subsection 3.4. First, a reference baseline was established by simulating an empty wind tunnel, and then the force plate sensor and the smoke injector where placed in the test section one at a time while the change in the flow was observed.

The results of reference case in the form of cut-planes graphing velocity magnitude and turbulence intensity both parallel to the flow and perpendicular to the flow at the middle of the test section is found in Fig.C.3 and Fig.C.4 in Appendix C.

#### 4.1 Force plate sensor

When the force plate sensor was added to the floor of the wind tunnel test section, equivalent graphs was created for the velocity magnitude and the turbulence intensity, as seen in Fig.5 and Fig.6.

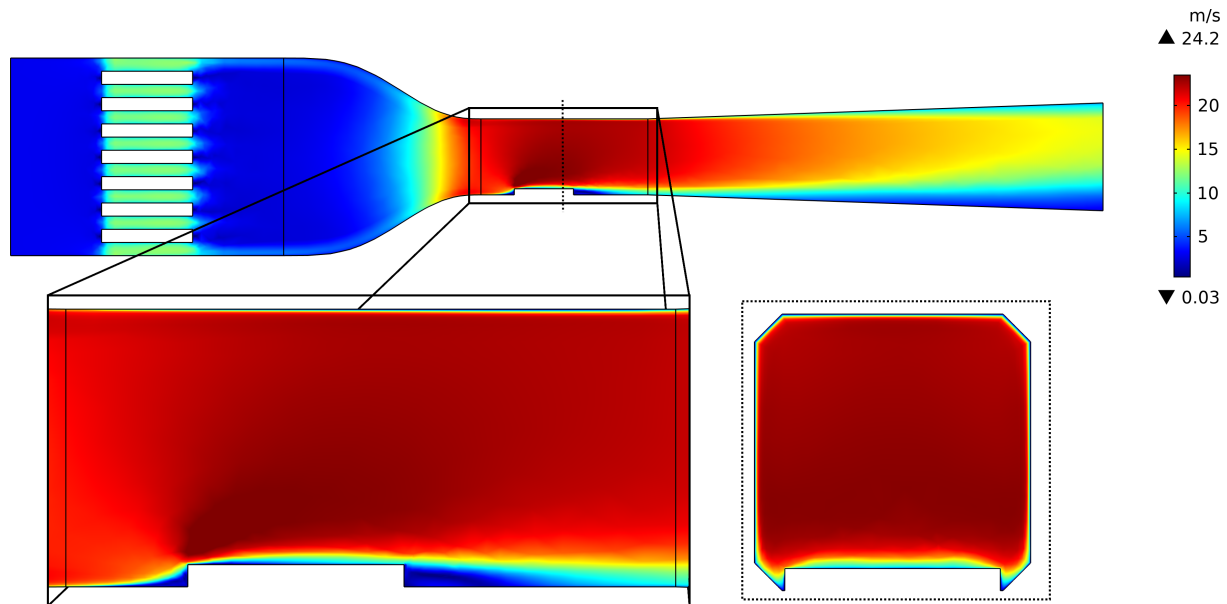


**Figure 5** – Cut-planes showing velocity magnitude with the force sensor added.

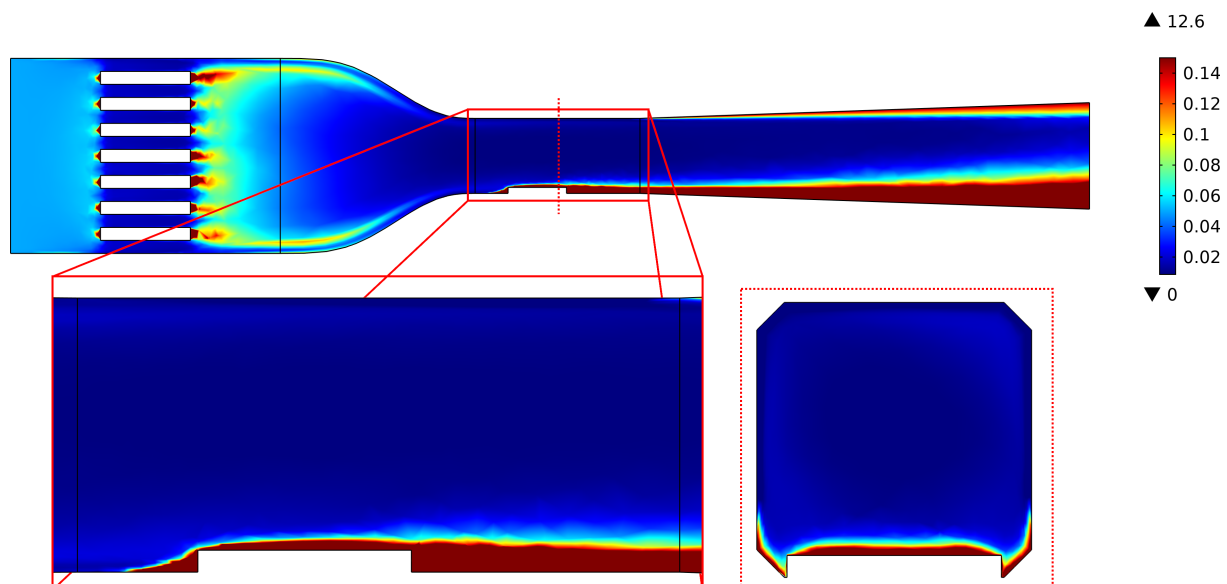


**Figure 6** – Cut-planes showing turbulence intensity with the force sensor added.

In the first figure displaying cut-planes of the velocity magnitude, one can observe how separation bubbles are forming in front of and behind the force plate sensor, as the flow is

restricted and slowed down by the sharp edges of the sensor [3]. The non-smooth geometry of the force plate sensor gives rise to an increased adverse pressure gradient, which causes the flow to separate from the wall and small re-circulation regions are formed both in front and behind the sensor. Additionally, due to conservation of mass in the incompressible flow, the main bulk flow is as a result of the constriction sped up in the test section and downstream from the sensor, compared to the reference case with an empty tunnel.

In the second figure showing cut-planes of the turbulence intensity with the force sensor added, it is apparent how the rough edges of the sensor geometry causes the turbulent boundary layer at the wall to increase dramatically in size and fully detach from the wall. Even though the turbulence levels does not seem to be very affected far from the plate sensor, one can clearly observe how lots of turbulence is generated in the flow passing over the sensor and being carried downstream while slowly diffusing out into the main bulk flow.

## 4.2 Smoke injector

Next up, we simulate flow in the wind tunnel when the smoke injector has been added to the test section. Graphs showing cut-planes of the velocity magnitude and turbulence intensity can be seen in Fig.7 and Fig.8.

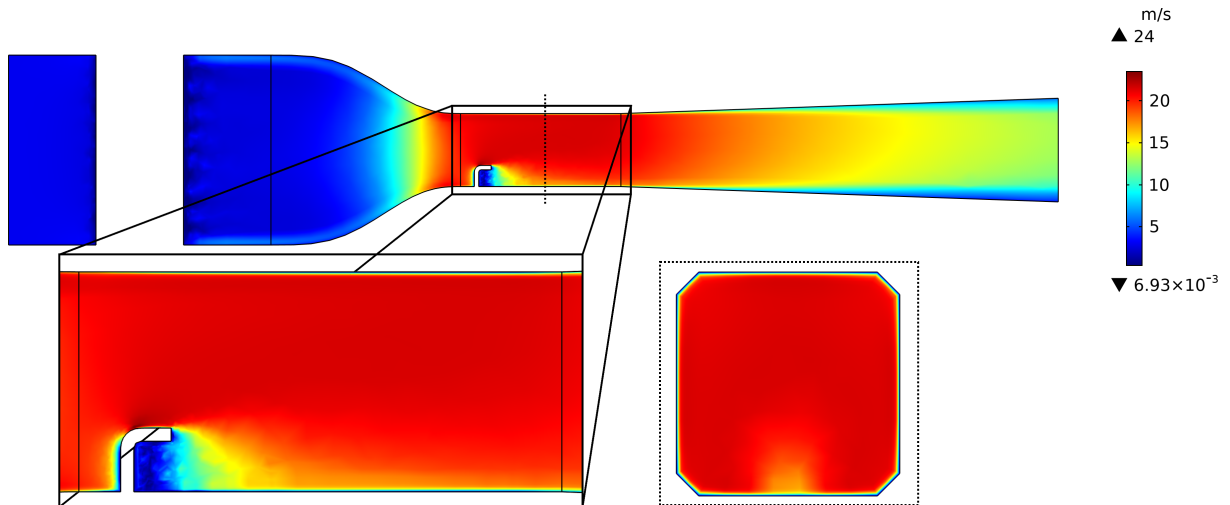


**Figure 7 –** Cut-planes showing velocity magnitude with the smoke injector added.

In the first figure, similarly to the case of the force plate sensor, one may see how separation bubbles are created in front and behind the smoke injector as flow is hindered and slowed down by its presence. A wake is formed behind the smoke injector, but it is much smaller in size than that of the force sensor, likely due to the much smaller size of the injector. Also, there is not as much flow separation occurring downstream from the smoke injector.

In the second figure, where turbulence intensity is graphed for the flow around the smoke injector, we notice a few things which is different to the case of the force plate sensor. Namely, there is very little boundary layer separation happening at the wind tunnel wall, unlike for the plate sensor. Granted, there is a wake behind the smoke injector which is a large source of turbulent kinetic energy, and this turbulence is carried downwind with the bulk of the flow. However, this turbulence seemingly dissipates relatively quickly and the turbulence intensity is returning to rather low levels a relatively short distance after leaving the smoke injector.

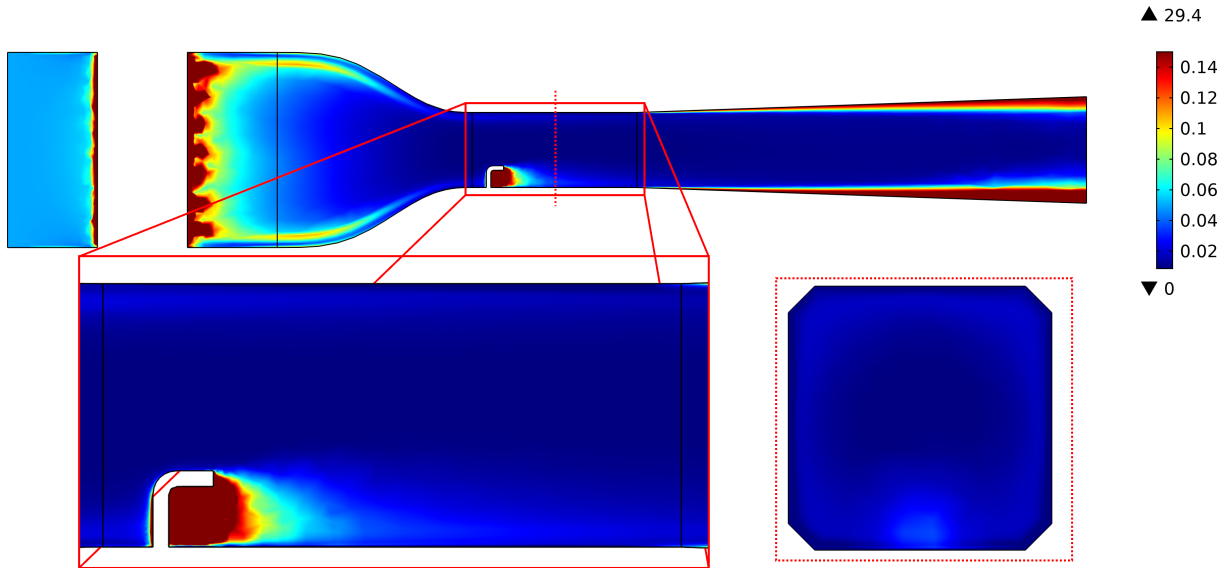


**Figure 8** – Cut-planes showing turbulence intensity with the smoke injector added.

### 4.3 Comparison with reference data

To gain a greater confidence in the validity of the simulation, we try to quantify and compare the obtained results with external reference data. The way we have chosen to achieve this is by calculating the dimensionless turbulence kinetic energy and the dimensionless mean flow velocity, as detailed in subsection 2.5, measured along the three vertical cut-lines shown in Fig.3. We then compare our obtained measurements with data obtained through Direct Numerical Simulations (DNS) by Kim *et al.* [8] and Bernardini *et al.* [9] for the case of fully developed 2D channel flow. The simulations performed in this study have had an Reynolds number of  $Re = 150000$  while having a Reynolds number based on the friction velocity as  $Re_\tau = 1250$ . The DNS performed by Kim *et al.* was done at  $Re = 7890$  and  $Re_\tau = 395$ , while the DNS conducted by Bernardini *et al.* was done with  $Re = 39600$  and  $Re_\tau = 1000$ . The comparison of DNS data with simulations results can be seen in Fig.9.

In the figure, one can see the three simulated cases does not entirely align with the reference data, but it does show some of the same trends and behaviour. The velocity profile of our simulated reference case does align well with the DNS data close to the wall, but diverts as the distance to the wall grows. This is likely due to the fact that both of the DNS datasets describe fully developed turbulent flows, meaning that the turbulent boundary layer has grown to an equilibrium width in the channel flow, while on the other hand, the design of the wind tunnel is specifically made with the intent of minimizing the turbulence intensity levels in the test section [1]. As such, design decisions have been made trying to reduce the turbulent boundary layers as much as possible and thus it is probable to be the reason for the discrepancy between our wind tunnel simulation and the DNS-data, since our simulation and DNS reference data agree well close to the wall where the boundary layer is situated. Further differences in the velocity profiles of the cases with the force sensor and the smoke injector is likely simply due to the disturbances these objects create themselves by their presence in the flow of the wind tunnel.

Furthermore, the graphs of the dimensionless turbulent kinetic energy in the figure are somewhat similar in character between the simulated cases and the DNS reference data, but they do not align closely. We argue that this is also due to the fact that we are comparing turbulent flow

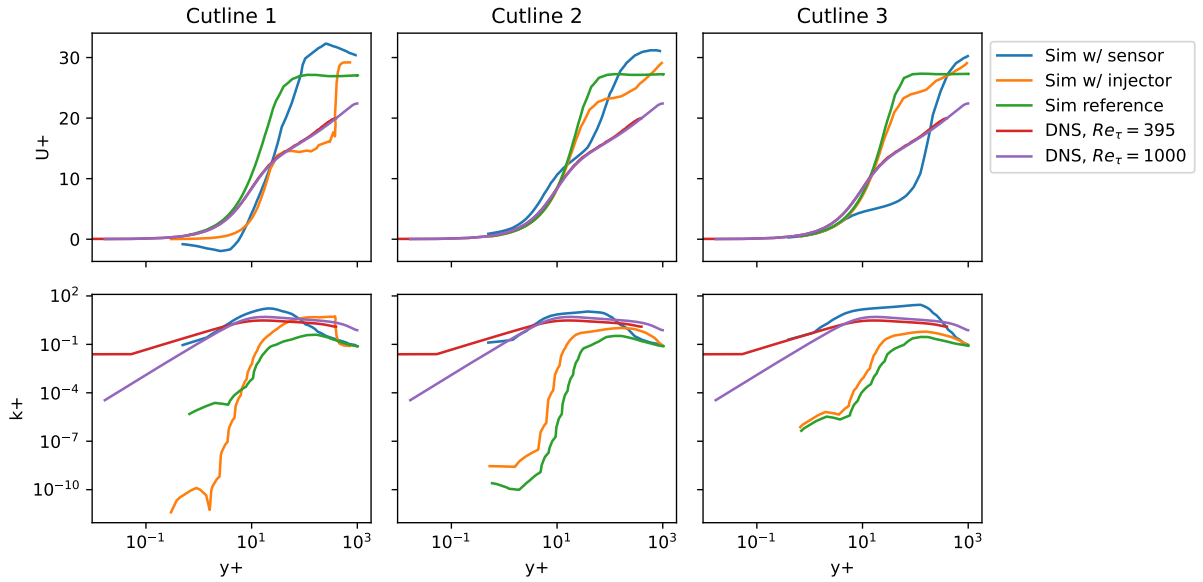


**Figure 9** – Comparison of dimensionless velocity  $U^+$  and turbulent kinetic energy  $k^+$  relative dimensionless distance from the wall  $y^+$ . Measured along the three vertical cut-lines placed in the test section, as detailed in subsection 3.3, for fluid flow with the force sensor or the smoke injector added, and the reference case with an empty tunnel. Additionally, the measurements are overlaid with DNS-data for 2D channel flow from Kim *et al.* [8] at  $Re_\tau = 395$  and Bernardini *et al.* [9] at  $Re_\tau = 1000$ .

which is fully developed and turbulent flow which is not. One indication which may strengthen this hypothesis is the fact that the graph of the turbulent kinetic energy has roughly the same “hill” shape, but rises to different heights. Thus if the test section tunnel was long enough for the flow to become fully developed, I believe that the turbulence kinetic energy in the boundary layer would continue to grow until it approximately filled the same contour as the DNS data.

## 5 Discussion

The aim of this study was to examine how the turbulence of the flow in the wind tunnel was affected by the addition of Hydroflux’s force plate sensor and smoke injector. As seen from the results of the previous section, the presence of the force plate sensor and the smoke injector does impact the flow, both near the objects themselves but also in the bulk flow of the test section. The force sensor generates boundary layer separation due to its rough and sharp geometry, which means that lots of turbulence is created near the sensor and carried by the flow downstream while slowly diffusing into the main bulk flow. This is an unwanted phenomena, since it would likely interfere and cause disturbances with any experiments conducted in the wind tunnel [1]. Unless the base geometry of the force plate sensor could be altered, the suggestion would be to lessen the impact by extending the geometry and making more suited from an aerodynamics standpoint, e.g. by designing a gradual rise and fall at the back and front of the force sensor, optimally without any sharp edges and a gradual enough slope to avoid any boundary layer separation at the target flow rate of the wind tunnel [1], [4]. Further studies could investigate the optimal shape and dimensions for such an extension to the force plate sensor.

Furthermore, the inclusion of the smoke injector in the wind tunnel did also introduce additional

turbulence in the flow of the wind tunnel, although it did not create boundary layer separation to the same extent as for the force sensor. Thus, we would additionally suggest further studies which may determine ways to minimize the impact of the smoke injector on the flow. Such improvement may likely involve to the introduction of a leading edge at the front of the smoke injector which presents less of a blockade for the fluid flow, and a trailing edge which should help alleviate boundary separation behind the smoke injector. Such measures could have the potential to reduce the wake behind the injector and thus lessen the impact it has on the flow in the wind tunnel.

Although the numerical methods used to simulate fluid dynamics in this investigation are not by any means the most accurate and advanced available, they present a good trade-off between being physically sound while being computationally attainable given the available time and scope of the investigation. The mesh convergence study performed gave confidence in the chosen mesh quality and resolution, such that the simulation would produce results which are physically reasonable. Additionally, validations of our simulation setup was done with comparisons to numerical reference data obtained through DNS of turbulent flow in a 2D channel, with relatively satisfactory results. Even if there were differences between the DNS reference case and our simulation setup, such as the DNS data conveying fully developed turbulent flow while the wind tunnel simulation is not, none of the behaviour graphed clearly indicated any strong reason to distrust the simulation results.

However, since it is hard to come by high resolution simulations or DNS:s of the same or similar wind tunnel setup as in our case, the only sure-fire way to validate the design and performance of the wind tunnel and the sensor and smoke injector is to actually build the real-life wind tunnel, run the desired tests. Thus, being confined to solely numerical methods will only provide you with a limited amount of confidence before the same design has been thoroughly evaluated in real, physical fluid flow [1]. Nonetheless, performing these initial numerical investigations can prove to be a quick and cost-effective way to iterate and improve potential designs before the costly process of constructing the wind tunnel has to take place.

## 6 Conclusion

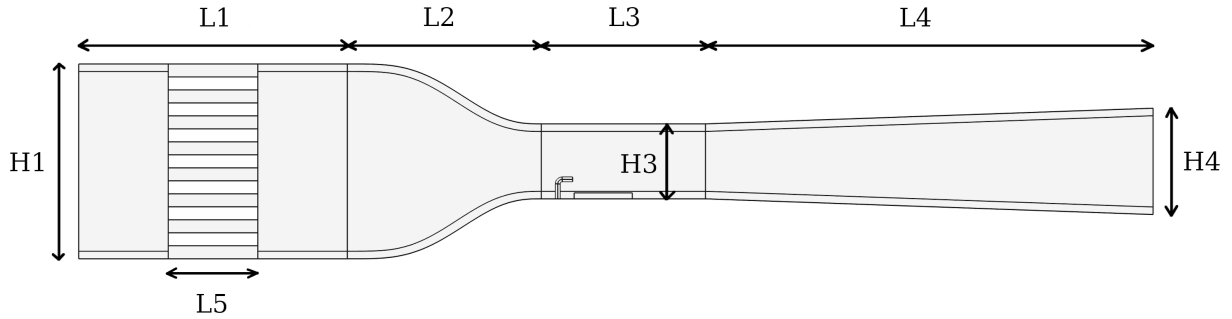
Text here.

## References

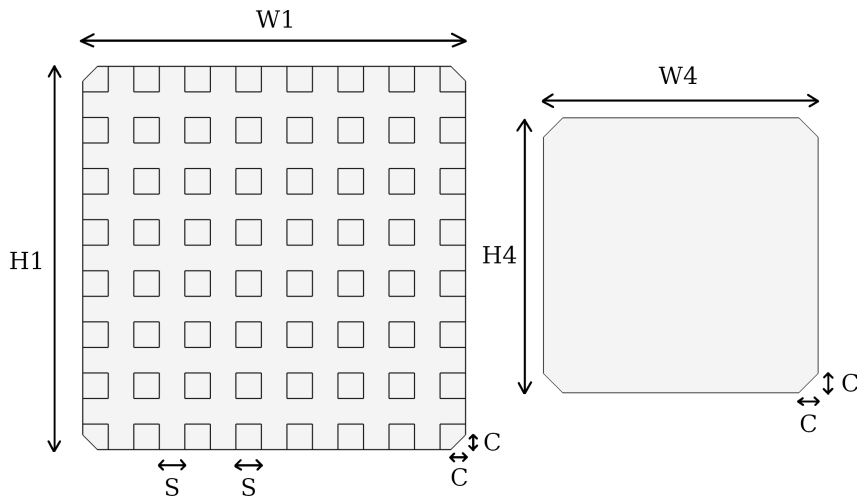
- [1] L. Cattafesta, C. Bahr, and J. Mathew, “Fundamentals of wind-tunnel design,” in *Encyclopedia of Aerospace Engineering*, R. Blockley and W. Shyy, Eds., Chichester, UK: John Wiley & Sons, Ltd, Dec. 15, 2010, eae532. DOI: 10.1002/9780470686652.eae532.
- [2] J. Sargison, G. Walker, and R. Rossi, “Design and calibration of a wind tunnel with a two dimensional contraction,” presented at the 15th Australasian Fluid Mechanics Conference, The University of Sydney, Sydney, Australia: University of Tasmania, Dec. 13, 2004.
- [3] P. A. Davidson, *Turbulence: an introduction for scientists and engineers*, Second edition. Oxford, United Kingdom ; New York, NY, United States of America: Oxford University Press, 2015, 630 pp., OCLC: ocn911091654.
- [4] S. Mauro, S. Brusca, R. Lanzafame, F. Famoso, A. Galvagno, and M. Messina, “Small-scale open-circuit wind tunnel: Design criteria, construction and calibration,” *International Journal of Applied Engineering Research*, vol. 12, no. 23, pp. 13 649–13 662, 2017.
- [5] E.-S. Zanoun, “Flow characteristics in low-speed wind tunnel contractions: Simulation and testing,” *Alexandria Engineering Journal*, vol. 57, no. 4, pp. 2265–2277, Dec. 2018. DOI: 10.1016/j.aej.2017.08.024.
- [6] F. G. Schmitt, “About boussinesq’s turbulent viscosity hypothesis: Historical remarks and a direct evaluation of its validity,” *Comptes Rendus Mécanique*, vol. 335, no. 9, p. 617, Oct. 2007. DOI: 10.1016/j.crme.2007.08.004.
- [7] K. Abe, T. Kondoh, and Y. Nagano, “A new turbulence model for predicting fluid flow and heat transfer in separating and reattaching flows—i. flow field calculations,” *International Journal of Heat and Mass Transfer*, vol. 37, no. 1, pp. 139–151, Jan. 1, 1994. DOI: 10.1016/0017-9310(94)90168-6.
- [8] J. Kim, P. Moin, and R. Moser, “Turbulence statistics in fully developed channel flow at low reynolds number,” *Journal of Fluid Mechanics*, vol. 177, pp. 133–166, Apr. 1987, Publisher: Cambridge University Press. DOI: 10.1017/S0022112087000892.
- [9] M. Bernardini, S. Pirozzoli, and P. Orlandi, “Velocity statistics in turbulent channel flow up to  $re_{tau}=4000$ ,” *Journal of Fluid Mechanics*, vol. 742, pp. 171–191, Mar. 2014, Publisher: Cambridge University Press. DOI: 10.1017/jfm.2013.674.

## A Appendix: Wind tunnel dimensions

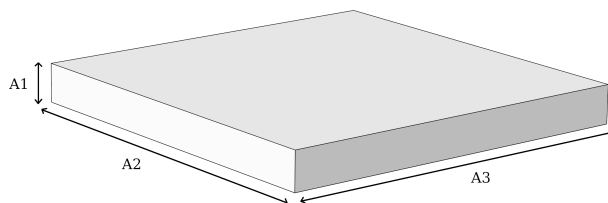
The final wind tunnel geometry used in this study follows the schematics shown in Fig.A.1 and Fig.A.2 with the chosen specifications as listed in Tab.A.1. Placed in the test section of the wind tunnel, we have the plate force sensor as described in Fig.A.3 and the smoke injector as shown in Fig.A.4, together with the specifications as listed in Tab.A.2.



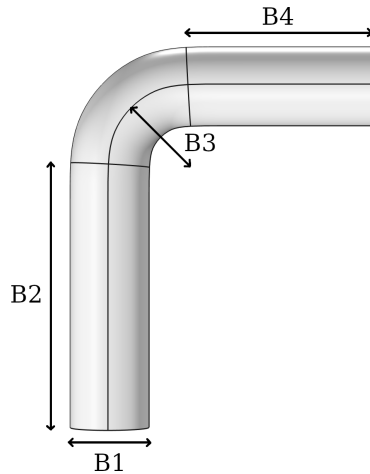
**Figure A.1** – Side view of the wind tunnel, with the force sensor and smoke injector included. Flow is directed horizontally from the left to right hand side of the figure.



**Figure A.2** – Cross sections of the wind tunnel, flow direction is into the figure. Left: comb of the settling chamber. Right: outlet at the end of the diffuser.



**Figure A.3** – Schematic of the force sensor.

**Figure A.4** – Schematic of the smoke injector.**Table A.1** – Dimensions used for the wind tunnel.

Dimension	Size [mm]	Comment
L1	180	Length of settling chamber
L2	130	Length of contraction
L3	110	Length of test section
L4	300	Length of diffuser
L4	60	Length of flow settling comb
H1	130	Height of inlet to the settling chamber
H3	50	Height of inlet to test section
H4	71	Height of outlet from diffuser
W1	130	Width of settling chamber
W3	50	Width of test section
W4	71	Width of diffuser at outlet
S	1/15*H1	Element width of flow settling comb
C	5	Width of 45° chamfer

**Table A.2** – Dimensions used for the force sensor and the smoke injector.

Dimension	Size [mm]	Comment
A1	4	Force sensor height
A2	39	Force sensor depth
A3	39	Force sensor length
B1	3	Injector diameter
B2	10	Injector vertical length
B3	3	Injector bend radius
B4	10	Injector horizontal length

## B Appendix: Contraction shape

The design of the contraction section of the wind tunnel has been guided by Sargison *et al.* [2], with the recommendation of a contraction ratio from Zanoun [5]. In [2], a sixth order polynomial on the form

$$y = ax^6 + bx^5 + cx^4 + dx^3 + ex^2 + fx + g, \quad (\text{B.1})$$

is chosen to represent the curvature of the contraction section, and seven constraints are applied in order to solve for the optimal shape. The procedure of solving the system of equations to generate the curvature shape is detailed in the Matlab-script found below.

However, as discussed in subsection 3.2, the initial design of the contraction section provided by Hydroflux AB contained a small logical error which resulted in a sub-optimal fit in the connection between the contraction and test section. Thus, both the original and the improved parameters for the curvature is listed in Tab.B.1. Note that only the improved contraction design has been used during the investigation of the force sensor and smoke injector.

**Table B.1** – Coefficients determining the shape of the contraction section, corresponding to Equation B.1. Original values supplied by Hydroflux AB as well as the improved values of the modified geometry are listed.

Parameter	Original design	Improved design	Comment
CR	7	6.76	Contraction ratio
a	$-7.6770 \cdot 10^4$	$-8.2870 \cdot 10^4$	
b	$2.4374 \cdot 10^4$	$2.5856 \cdot 10^4$	
c	$-2.0152 \cdot 10^3$	$-2.1008 \cdot 10^3$	
d	$3.3626 \cdot 10^{-12}$	$-2.0664 \cdot 10^{-13}$	
e	0	0	
f	0	0	
g	-	-	Vertical offset

```

clear all
% Script based on the original work provided by Hydroflux AB.
% Modified by Elias Olofsson.
%
% Changelog:
% v1.0 2021-12-05: Author: Hydroflux AB.
% Publication of original work.
% v2.0 2022-01-14: Author: Elias Olofsson.
% Changed order of operations such to make flush connections with settling
% chamber and test section of predetermined widths. Now CR is determined by
% the ratio of Di to Do, where in the previous version, Di where allowed
% to vary to fit a certain specified value of CR.
%
% Design of wind tunnel contraction shape based on the following two papers:
% [1] "Design and calibration of a wind tunnel with a two dimensional
% contraction", J.E. Sargison, G.J. Walker and R. Rossi, 2004
% [2] "Flow characteristics in low-speed wind tunnel contractions: Simulation and
% testing", Alexandria Engineering Journal (2018) 57
% Following [1] a sixth order polynom is chosen as shape model for a
% 2D-contraction with inlet crosssection Di*W, outlet crosssection Do*W:
% y=a*x^6+b*x^5+c*x^4+d*x^3+e*x^2+f*x+g
% From [2] the recommendation of contraction number CR is between 6-12
% and the contraction length L is between 0.75*Di and 1.25*Di
% CR is chosen to 5, i.e. CR=(Di*W)/(Do*W)=5
% and the contraction length is chosen to L=Di

```

```
% Model 3 in [1] is chosen, i.e xi/L=0.6 and alpha=0, where xi is the
% inflexion point along contraction axis and alpha is the inlet curvature.

Do=0.050; %50mm
Di=0.130; %130mm
CR = Di^2/Do^2
L=1.0*Di;
xi=0.6*L;
h=1*(Di/2-Do/2);

% The constraints on the shape model is the following:
% x=0: y(0)=h, y'(0)=0, y''(0)=0
% x=L: y(L)=0, y'(L)=0, y''(L)=0
% x=xi: y''(xi)=0
% When the constraints are applied we obtain a system of equations
% for the coefficients a,b,c,d in terms of L and xi, and that g=h, f=e=0.
% The system looks like Asys*Coeff=B:

Asys=[30*xi^4 20*xi^3 12*xi^2 6*xi;
L^6 L^5 L^4 L^3;
6*L^5 5*L^4 4*L^3 3*L^2;
30*L^4 20*L^3 12*L^2 6*L];
B=[0 -h 0 0]';
Coeff=linsolve(Asys,B);
a=Coeff(1); b=Coeff(2); c=Coeff(3); d=Coeff(4); e=0; f=0; g=h;
%Contraction shape model from [1]
x=[0:0.001:L];
y=a*x.^6+b*x.^5+c*x.^4+d*x.^3+e*x.^2+f*x+g;

%Plot shape
figure(1)
hold on
plot(x,y+Do/2,'b')
plot(x,-y-Do/2,'b')
xlabel('x'); ylabel('y'); axis equal
title(['CR=', num2str(CR), ', L/Di=', num2str(L/Di)])
```

## C Appendix: Validation of modifications to geometry

Due to reasons presented in subsection 3.2, the modifications to the original wind tunnel design provided by Hydroflux AB must be justified and validated. Two simulation runs performed at a high mesh quality as specified in subsection 3.4 were performed for each of the two geometries; the original and the modified design.

The velocity profile of the original Hydroflux design can be seen in Fig.C.1, graphed along the slightly off-center cut-plane parallel to the flow as well as through the cut-plane perpendicular to the flow at the center of the test section. As one can see in the figure, the flow forms a small separation bubble [3] as it passes over the small 'lip' at the intersection between the contraction and the test section. This generates a small boundary layer which propagates down the test section, widening as it travels downstream. Furthermore, in the cut-plane perpendicular to the flow, one can note that the square edges of the rectangular cross-section of the wind tunnel seem to be a source of flow slow-down and separation, as predicted by [2].

Next, we graph the turbulence intensity for the original geometry, as seen in Fig.C.2. Here, one can see the creation of turbulence generated by the small 'lip' between the contraction and the test section, as well as at the square corners of the wind tunnel cross-section perpendicular to the flow.

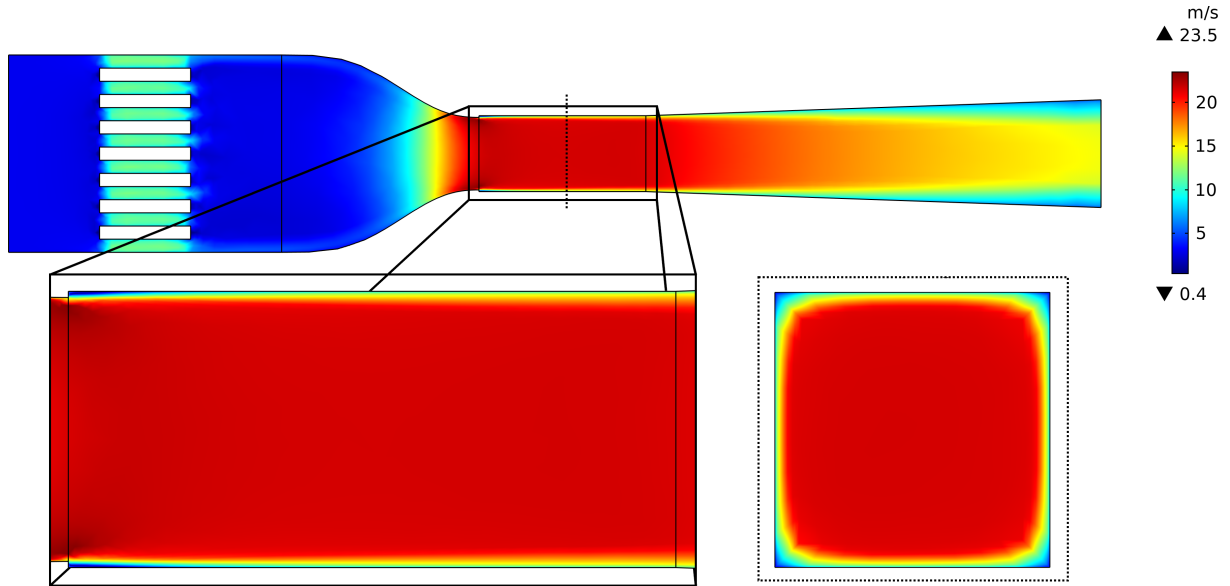


**Figure C.1** – Cut-planes showing velocity magnitude for the original geometry.

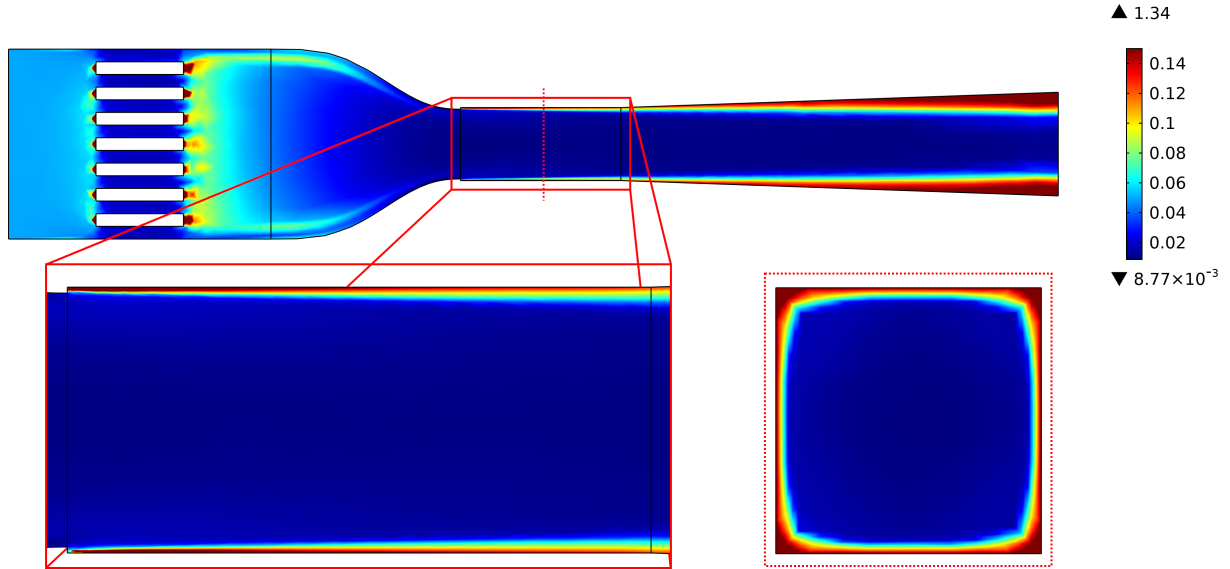


**Figure C.2** – Cut-planes showing turbulence intensity for the original geometry.

For the second simulation, we evaluate the modified design on an equivalent mesh, as specified in subsection 3.2, Appendix A and Appendix B. Cut-planes of the velocity magnitude can be seen in Fig.C.3, also plotted along the slightly off-center cut-plane parallel to the flow and perpendicular to the flow. Here, one can see a decrease in boundary layer separation, likely due to the removal of the slight 'lip' at the intersection between contraction and test section of the original design. Additionally, the flow separation at the square corners of the perpendicular cross-section of the wind tunnel have been dramatically reduced, likely due to the introduction of 45° chamfers along the wind tunnel corners.

Moreover, we can see in the equivalent graph of the turbulence intensity along the cut-planes, as seen in Fig.C.4, that turbulence levels have decreased relative to the original design. The boundary layer with turbulence is thinner than in the original geometry, and additionally that turbulence levels have lowered in the corners of the wind tunnel cross-section.

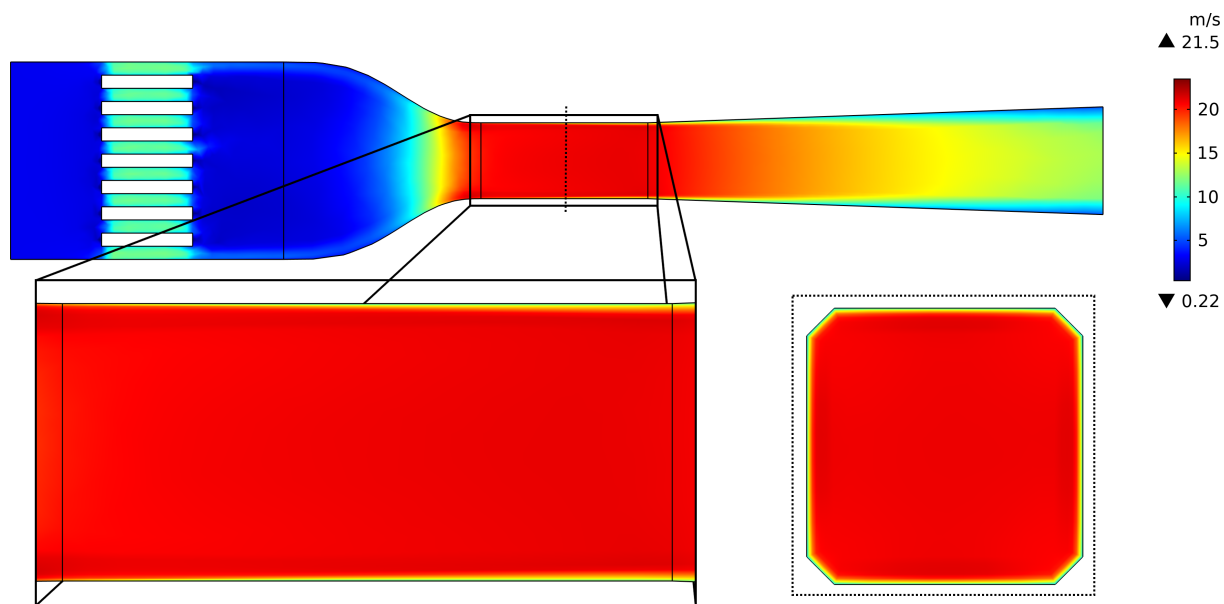


**Figure C.3 –**Cut-planes showing velocity magnitude for the modified geometry.

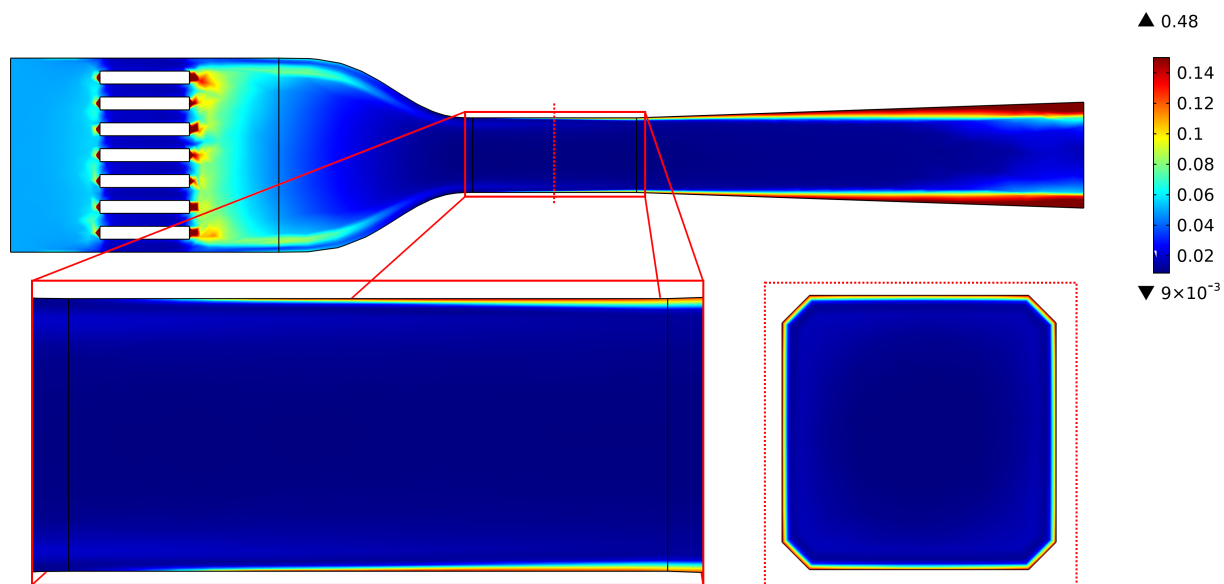


**Figure C.4 –**Cut-planes showing turbulence intensity for the modified geometry.

As such, all other investigations conducted in this study have been performed with the modified geometry, which introduced  $45^\circ$  chamfers and a slight error-correction in the shape of the contraction section, for the elimination of a small miss-alignment between the the contraction and test section.